



# CHORUS

This is the accepted manuscript made available via CHORUS. The article has been published as:

## Universal link of magnetic exchange and structural behavior under pressure in chromium spinels

Ilias Efthimiopoulos, Indiras Khatri, Zhi T. Y. Liu, Sanjay V. Khare, Pankaj Sarin, Vladimir Tsurkan, Alois Loidl, Dongzhou Zhang, and Yuejian Wang

Phys. Rev. B **97**, 184435 — Published 31 May 2018

DOI: [10.1103/PhysRevB.97.184435](https://doi.org/10.1103/PhysRevB.97.184435)

# Universal link of magnetic exchange and structural behavior under pressure in chromium spinels

*Ilias Efthimiopoulos<sup>a,b,1,2</sup>, Indiras Khatri<sup>c,2</sup>, Zhi T. Y. Liu<sup>c</sup>, Sanjay V. Khare<sup>c</sup>, Pankaj Sarin<sup>d</sup>,  
Vladimir Tsurkan<sup>e</sup>, Alois Loidl<sup>e</sup>, Dongzhou Zhang<sup>f</sup>, and Yuejian Wang<sup>a,1</sup>*

<sup>a</sup>Department of Physics, Oakland University, Rochester, Michigan 48309, USA

<sup>b</sup>Deutsches GeoForschungsZentrum, Section 4.3, Telegrafenberg, 14473, Potsdam, Germany

<sup>c</sup>Department of Physics and Astronomy, University of Toledo, Toledo, Ohio 43606, USA

<sup>d</sup>School of Materials Science and Engineering, Oklahoma State University, Tulsa, Oklahoma 74106, USA

<sup>e</sup>E. P. V, Center for Electronic Correlations and Magnetism, University of Augsburg, 86159 Augsburg, Germany

<sup>f</sup>Partnership for Extreme Crystallography, University of Hawaii at Manoa, Honolulu, Hawaii 96822, USA

We have conducted high-pressure X-ray diffraction studies on the  $\text{MnCr}_2\text{O}_4$  and  $\text{NiCr}_2\text{O}_4$  spinels at room temperature. Both compounds undergo pressure-induced structural transitions into diverse tetragonal modifications. Based on these experimental observations and our *ab initio* calculations, we show that the Cr-oxide spinels with magnetic  $A^{2+}$  cations ( $A^{2+} = \text{Mn, Fe, Co, Ni}$ ) follow a similar trend as their chalcogenide counterparts with non-magnetic  $A^{2+}$  ions, i.e. the transition pressure is proportionally related with the magnitude of the Cr-Cr magnetic exchange interactions. Therefore, we reach the conclusion that *the Cr-Cr magnetic exchange interactions alone suffice to account for the high-pressure behavior of these systems*. Our results clearly depict the close relationship between the structural and magnetic degrees of freedom in Cr-bearing spinels.

**PACS number(s): 61.50.Ks, 75.50.Pp, 71.20.-b**

<sup>1</sup>Corresponding authors: [ilias.efthymiopoulos@gfz-potsdam.de](mailto:ilias.efthymiopoulos@gfz-potsdam.de) and [ywang235@oakland.edu](mailto:ywang235@oakland.edu)

<sup>2</sup>These authors contributed equally to this work.

## I. INTRODUCTION

The series of  $A^{2+}Cr^{3+}_2X_4$  ( $A^{2+} = Mn-Zn, Cd, Hg; X = O, S, Se$ ) spinels (SG  $Fd\bar{3}m$ ,  $Z = 8$ ) constitutes an ideal system for studying magnetic exchange interactions in solids<sup>1-3</sup>. The spinel structure is composed of edge-sharing  $Cr^{3+}$  octahedral units with six nearest neighbors/anions (the  $Cr^{3+}$  cations themselves form tetrahedral in a pyrochlore-type lattice, thus allowing for magnetic frustration) and relatively ‘isolated’  $A^{2+}$  tetrahedral units with four nearest neighbors (Fig. 1).

Depending on the type and size of the tetrahedrally coordinated  $A^{2+}$  cations and the corresponding anions, the magnetic exchange interactions can vary significantly<sup>3,4</sup>. As established already in the 1960s<sup>5-8</sup>, spinels with non-magnetic  $A^{2+}$  cations may exhibit either direct  $Cr^{3+}-Cr^{3+}$  antiferromagnetic (AFM) or indirect ferromagnetic (FM) Cr-X-Cr interactions depending on the  $Cr^{3+}-Cr^{3+}$  distance. The AFM interactions are dominant in the Cr-spinel oxides with smaller  $Cr^{3+}-Cr^{3+}$  distances; on the other hand, the Cr-X-Cr FM exchange prevails in the Cr-bearing sulfide and selenide spinel series due to the higher  $Cr^{3+}-Cr^{3+}$  separation distances compared to the oxides<sup>6,8-10</sup>. This fact alone indicates the strong coupling between magnetism and structure in these compounds. Indeed, several experimental studies have showed the enhancement of the AFM interactions upon decreasing the  $Cr^{3+}-Cr^{3+}$  distances, via the reduction of the Cr-spinel volume under external compression<sup>11,12</sup>. **In certain cases, electronic changes, e.g. insulator-to-metal<sup>13-16</sup> or semiconductor-to-semiconductor<sup>17</sup> transitions have been reported.** On the other hand, the magnetic interactions of the oxide spinels with magnetic  $A^{2+}$  cations are more complex, since one needs to consider also the  $A^{2+}-Cr^{3+}$  and the more distant  $A^{2+}-A^{2+}$  magnetic exchange interactions<sup>2,4,18</sup>.

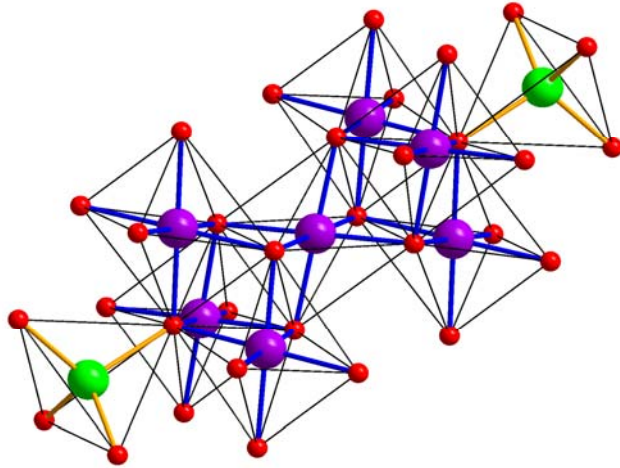


**FIG. 1.** The crystal structure of the  $A^{2+}Cr^{3+}_2O_4$  spinel compounds ( $A^{2+} = Mn-Zn, Cd, Hg$ ). The A, Cr, and oxygen atoms are shaded in green, purple and red, respectively.

In previous works we have unraveled the close correlation between the magnetic exchange interactions and the pressure-induced structural transitions in  $ACr_2X_4$  Cr-spinel chalcogenides with non-magnetic  $A^{2+}$  cations ( $A = Zn, Cd, Hg; X = S, Se$ )<sup>19,20</sup>. In particular, we have shown that the ratio of the next-nearest neighbor ( $K_{nnn}$ ) over the nearest neighbor ( $J_{nn}$ ) magnetic interactions is proportional to the structural transition pressure ( $P_{Tr}$ ) from the starting cubic  $Fd\bar{3}m$  phase towards a tetragonal modification<sup>21,22</sup>. Notable exceptions from this trend are  $ZnCr_2Se_4$ <sup>23</sup> and  $CuCr_2Se_4$ <sup>24</sup>, as their high-pressure behavior appears to be dictated by the similar ionic radii of tetrahedrally coordinated  $Zn^{2+}$  and  $Cu^{2+}$  with the octahedrally coordinated  $Cr^{3+}$ , and the higher covalency of the larger-sized Se anions [for a more detailed discussion see Ref.<sup>24</sup>]. Here we expand this idea to Cr-oxide spinels with magnetic  $A^{2+}$  cations ( $A^{2+} = Mn-Cu$ ). For this purpose, we have investigated the high-pressure structural behavior of  $MnCr_2O_4$  and  $NiCr_2O_4$  spinels by means of X-ray diffraction (XRD) and density functional theory (DFT)-based calculations. Combined with results from the literature, we could find a clear correlation between the Cr-Cr magnetic exchange interactions and  $P_{Tr}$  in these systems, as we describe below.

## II. EXPERIMENTAL AND COMPUTATIONAL DETAILS

The  $MnCr_2O_4$  and  $NiCr_2O_4$  single-crystalline samples have been synthesized with solid state reaction, as reported elsewhere<sup>25,26</sup>. The high pressure sample environment was generated by rhenium gasketed diamond anvil cells, equipped with diamonds of 300  $\mu m$  culet diameter. The ruby luminescence method was employed for pressure calibration<sup>27</sup>. The angle-resolved high-pressure powder XRD measurements were performed at the 16BM-D beamline of the High Pressure Collaborative Access Team ( $MnCr_2O_4$ ), and the 13-BMC beamline of the GeoSoilEnviroCARS ( $NiCr_2O_4$ ) at the Advanced Photon Source of Argonne National Laboratory<sup>28</sup>. The incident monochromatic X-ray beam energies were  $E = 29.2$  keV ( $\lambda = 0.4246$  Å,  $MnCr_2O_4$ ) and  $E = 28.6$  keV ( $\lambda = 0.434$  Å,  $NiCr_2O_4$ ). Helium served as a pressure transmitting medium in both experiments.

The majority of the measured XRD patterns were fitted with the Rietveld method. The refined parameters in each case were the lattice parameters, the atomic coordinates (Mn, Ni, and Cr reside in fixed positions in the ambient-pressure structures), and the profile parameters of the Stephens peak function<sup>29</sup>, whereas the background was modelled with a Chebyshev polynomial. Since the diffractograms showed textured rings, we employed a spherical harmonics correction<sup>30</sup> in order to account for the preferred orientation of the powder particles.

Our density functional theory (DFT) based calculations have been performed with the Vienna Ab initio Simulation Package<sup>31-34</sup>, using projector-augmented wave method<sup>35,36</sup> with the Perdew-Burke-Ernzerhof (PBE) generalized gradient approximation (GGA)<sup>37</sup>. The GGA+U correction scheme was used for the  $d$  orbitals of Mn, Ni, and Cr. The U values were chosen to be 3.9 eV for

Mn, 6.2 eV for Ni, and 3.7 eV for Cr<sup>38,39</sup>. Plane wave basis with appropriate k-point meshes and Gaussian smearing was used. We carefully constructed the cells with various magnetic configurations, including random solid solutions<sup>40,41</sup> provided in the Alloy Theoretic Automated Toolkit<sup>42,43</sup>. In each run the cell shape and atomic positions were allowed to freely relax as in earlier works<sup>23,44,45</sup>. To determine the magnetic exchange interactions parameters, we have calculated the total energies of various different magnetic configurations. Detailed quantitative descriptions of the above computational methods are provided in the the **Supplement**<sup>46</sup>.

### III. RESULTS AND DISCUSSION

#### A. Cubic MnCr<sub>2</sub>O<sub>4</sub> under pressure

In **Fig. 2(a)** we present XRD patterns of MnCr<sub>2</sub>O<sub>4</sub> at selected pressures. At ambient conditions, MnCr<sub>2</sub>O<sub>4</sub> crystallizes in the cubic spinel  $Fd\bar{3}m$  structure (**Fig. 1**). This ambient-pressure phase is retained up to ~8 GPa. Above this pressure, an abrupt broadening of the  $Fd\bar{3}m$  Bragg peaks is evidenced, as revealed by a change in the pressure dependence of the respective widths (**Fig. S1** in the **Supplement**<sup>46</sup>). Since we have used helium as pressure transmitting medium, we can most likely exclude non-hydrostatic effects at this relatively low pressure range<sup>47</sup>. Due to this Bragg peak broadening, the  $Fd\bar{3}m$  phase does no longer reproduce the XRD patterns satisfactorily; a tetragonal structure on the other hand, can reasonably index the measured diffractograms (**Fig. S1** in the **Supplement**<sup>46</sup>). **We note that upon passing from the cubic to the tetragonal structure, the majority of the  $Fd\bar{3}m$  Bragg peaks split into two or more components, thus accounting for the observed abrupt width broadening (Fig. S1 in the Supplement<sup>46</sup>).** Hence, we conclude that a cubic→tetragonal distortion takes place in MnCr<sub>2</sub>O<sub>4</sub> close to 8.3 GPa, similar to CoCr<sub>2</sub>O<sub>4</sub><sup>45</sup>. Due to this Bragg peak broadening, we could not assign a unique space group for this high-pressure tetragonal phase.

Further compression results in the appearance of a shoulder band in the Bragg peak located at ~8° close to 21 GPa [**Fig. 2(a)**]. This shoulder becomes more prominent with increasing pressure, at the expense of its adjacent Bragg peak. This observation is interpreted as a second structural transition, initiating at 21 GPa and completed at ~30 GPa [**Fig. 2(a)**]. This second-high-pressure phase can be also indexed to a tetragonal structure, with its *c*-axis reduced by 7.5% and its *a*-axis expanded by 4% compared to the first high-pressure tetragonal phase (**Table S1** in the **Supplement**<sup>46</sup>). Again due to the Bragg peak broadening, we could not assign a unique space group for this second high-pressure tetragonal phase. Further compression above 34 GPa appears to lead to an orthorhombic distortion (not shown); the pronounced broadening of the Bragg peaks, however, does not allow for reliable XRD refinements.

Due to the aforementioned Bragg peak broadening of our XRD patterns, we performed mostly Le Bail refinements for the majority of the MnCr<sub>2</sub>O<sub>4</sub> diffractograms. In **Fig. 2(b)** we plot the axial ratio of the tetragonal high-pressure phases of MnCr<sub>2</sub>O<sub>4</sub>; the respective lattice parameters

are provided in **Table S1** in the **Supplement**<sup>46</sup>. We can clearly observe that the cubic→tetragonal distortion is accompanied by a slight deviation from the cubic  $c/a$  unity value. On the other hand, the second pressure-induced tetragonal→tetragonal transition is manifested by an abrupt drop of the  $c/a$  axial ratio, owing to the sudden reduction of the tetragonal  $c$ -axis at the transition point (**Table S1** in the **Supplement**<sup>46</sup>). Such behavior is reminiscent of the documented pressure-induced structural transitions in several Cr-bearing spinels<sup>20,48</sup>. Nevertheless, both of the pressure-induced  $\text{MnCr}_2\text{O}_4$  structural transitions do not show any sizeable volume changes at the respective transition points [**Fig. 2(c)**]. The experimental  $P$ - $V$  data were fitted with Birch-Murnaghan equations of state<sup>49,50</sup>, with the respective results tabulated in **Table I**.

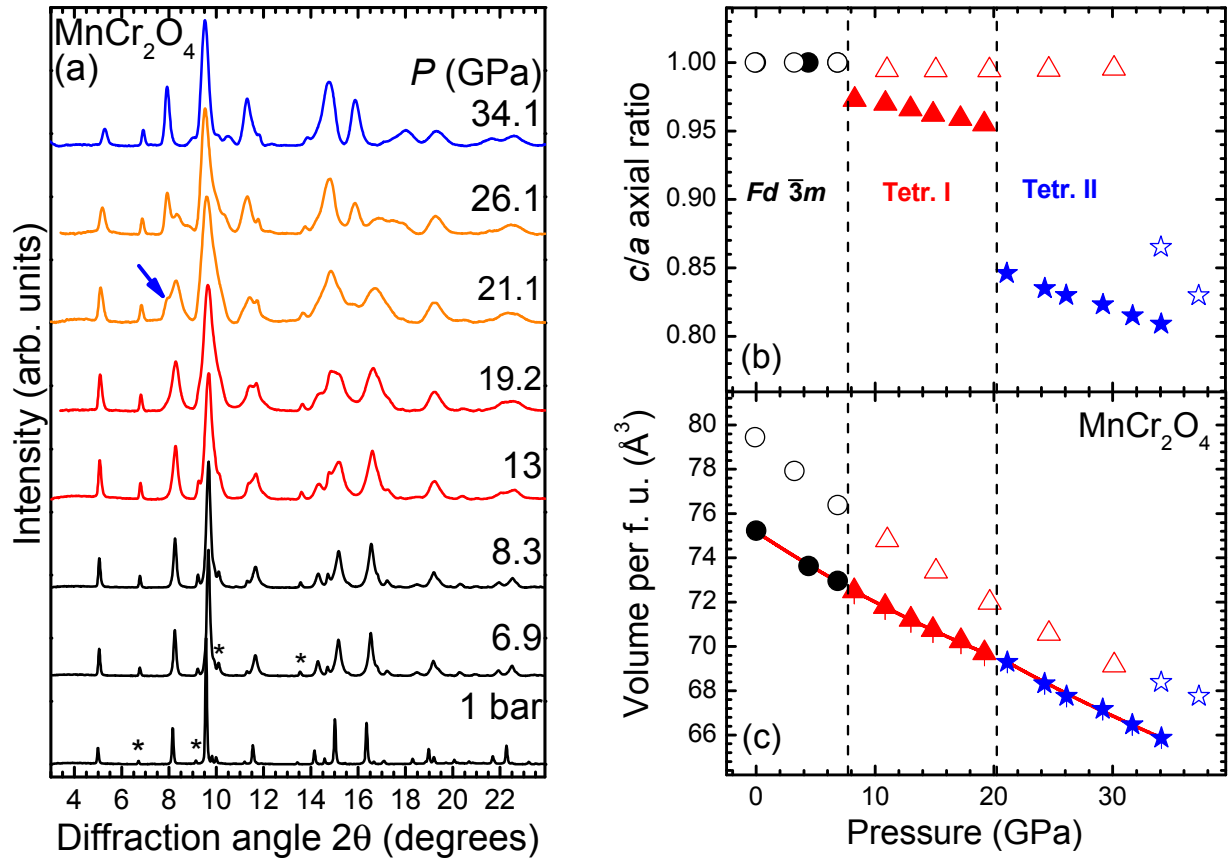


**FIG. 2.** (a) Selected XRD patterns of  $\text{MnCr}_2\text{O}_4$  at various pressures ( $T = 300$  K,  $\lambda = 0.4246$  Å). The various phases are distinguished by black ( $Fd\bar{3}m$ ), red (HP-tetragonal I), and blue (HP-tetragonal II) colors. Orange diffractograms denote the coexistence range. Asterisks mark the strongest Bragg peaks of the  $\text{Cr}_2\text{O}_3$  secondary phase. We also plot the (b)  $c/a$  axial ratio and (c) volume per formula unit (f. u.) as a function pressure for all phases of  $\text{MnCr}_2\text{O}_4$  (error bars lie within the symbols). The closed and open symbols correspond to experimental and DFT data, respectively. The vertical dashed lines depict the experimental transition pressures, and the red solid lines though the symbols indicate the fitted Birch-Murnaghan equations of state<sup>49,50</sup>. Black circles, red triangles, and blue stars correspond to the  $Fd\bar{3}m$ , the tetragonal AFM-MnCr, and the tetragonal

AFM-Cr phases of  $\text{MnCr}_2\text{O}_4$ , respectively, in both panels. The obtained elastic parameters are listed in **Table I**. The respective lattice parameters are provided in Tables **S1-S2** in the **Supplement**<sup>46</sup>.

In order to understand the origin behind these pressure-induced structural transitions, we have performed DFT calculations on  $\text{MnCr}_2\text{O}_4$  assuming a paramagnetic (PM) cubic structure and two different tetragonal AFM configurations, one with Mn spin-up and parallel to each Mn cation and Cr spin-down aligned parallel to each Cr cation but antiparallel to the Mn ones [similar to the experimental observation at ambient pressure<sup>51</sup>], and one with all  $\text{Mn}^{2+}$  in spin-up states, and half of  $\text{Cr}^{3+}$  in the same plane on the  $c$ -axis with spin-up states, the other half spin-down as in  $\text{CoCr}_2\text{O}_4$ <sup>45</sup> called AFM-MnCr and AFM-Cr, respectively (**Tables S2 & S3** in the **Supplement**<sup>46</sup>). From our calculations, we could find that the cubic $\rightarrow$ AFM-MnCr and the AFM-MnCr $\rightarrow$ AFM-Cr transitions take place at 17 GPa and 30.5 GPa, respectively (**Fig. 3** and **Fig. S2** in the **Supplement**<sup>46</sup>). Even though the experimental and calculated transition pressures exhibit discrepancies in their values, owing partially to the fact that DFT calculations are performed at 0 K and not at room temperature as the experiments, as well as the overestimation of the lattice parameters within the generalized gradient approximation (GGA) used here [see e.g. Ref. 52], we are confident that we have captured the main features of the observed  $\text{MnCr}_2\text{O}_4$  pressure-induced structural transitions, i.e. that both structural transitions are accompanied/triggered by changes in the magnetic properties of  $\text{MnCr}_2\text{O}_4$ . We will return back to this point later.

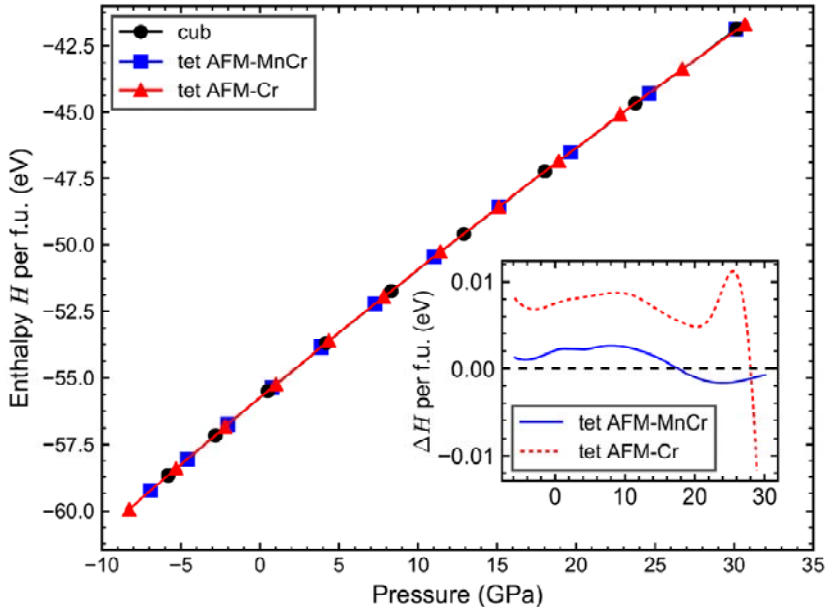


**FIG. 3:** The calculated enthalpies of the cubic paramagnetic (black), the tetragonal AFM1 (AFM-MnCr, blue) and tetragonal AFM2 (AFM-Cr, red) phases as a function of pressure. Inset: the enthalpy difference between the tetragonal AFM1 and AFM2 phases and the cubic phase with respect to pressure. Enthalpy  $H$  is defined as  $H(P) = E + PV$ , and a lower value of  $H$  indicates the phase

stability. The cubic→AFM-MnCr transition is calculated at 17 GPa (experimental value is 8.3 GPa). The AFM-MnCr→AFM-Cr transition is expected to take place at 30.5 GPa (extrapolated in Fig. S2 in the **Supplement**<sup>46</sup>, the experimental value is 21.1 GPa).

Despite the aforementioned transition pressure discrepancies, the calculated lattice parameters,  $c/a$  axial ratios, and the  $P$ - $V$  data for the various phases of  $\text{MnCr}_2\text{O}_4$  are qualitatively very similar to their experimental counterparts [Figs. 2 (b,c)]. We can immediately observe that the DFT calculated values lie always higher than their experimental counterparts, attributed to the tendency of the GGA approximation used here to overestimate the unit cell volumes and, concomitantly, underestimate the bulk moduli<sup>52</sup>.

**Table I:** Elastic parameters (volume  $V_{\text{Tr}}$ , bulk modulus  $B_{\text{Tr}}$ , and the pressure derivative of bulk modulus  $B'_{\text{Tr}}$ ) for the various phases of  $\text{MnCr}_2\text{O}_4$  and  $\text{NiCr}_2\text{O}_4$ , as obtained by a Birch-Murnaghan EoS<sup>49,50</sup>. Each parameter is evaluated at the transition pressure point  $P_{\text{Tr}}$ . N/A: Not available

Phase		$P_{\text{Tr}}$ (GPa)	$V_{\text{Tr}} / Z$ ( $\text{\AA}^3$ )	$B_{\text{Tr}}$ (GPa)	$B'_{\text{Tr}}$
$\text{MnCr}_2\text{O}_4$ $Fd\bar{3}m$	Exp.	$10^{-4}$	75.2(exp.)	212(5)	4(fixed)
	DFT (ParaM)		79.4	164.6	3.9
	Exp. <sup>53</sup>		75.5	180	N/A
$\text{MnCr}_2\text{O}_4$	Exp.	8.3	72.5(exp.)	230(6)	5.3(3)
HP1	DFT (AFM-MnCr)	17	72.8	164.1	4.5
$\text{MnCr}_2\text{O}_4$	Exp.	21.1	69.3(exp.)	231(3)	4(fixed)
	DFT (AFM-Cr)	30.5	69.5	164.3	3.9
$\text{NiCr}_2\text{O}_4$ $I4_1/amd$	Exp.	$10^{-4}$	71.9(exp.)	183(1)	4(fixed)
	DFT (ParaM)		73.9	165.3	3.3
	DFT (AFM)		75.5	166.5	3.6
$\text{NiCr}_2\text{O}_4$	Exp.	19.4	64(exp.)	182(6)	4.9(6)
$P4_32_12$	DFT (ParaM)	28.0	62.5	154.7	3.7
	DFT (AFM).	32.0	61.2	146.0	4.4

## B. Compression of Jahn-Teller active tetragonal $\text{NiCr}_2\text{O}_4$

Turning now to the high-pressure structural behavior of  $\text{NiCr}_2\text{O}_4$ , selected XRD patterns at various pressures are shown in Fig. 2(b). At ambient conditions,  $\text{NiCr}_2\text{O}_4$  adopts a tetragonal  $I4_1/amd$  structure ( $Z = 4$ ), a direct subgroup of the  $Fd\bar{3}m$  phase<sup>54</sup>, given the  $\text{Ni}^{2+}$  Jahn-Teller active ions<sup>55</sup>. Compression leads to changes in the XRD patterns starting at 19.4 GPa, with the most notable difference being the vanishing of the intense Bragg peak at  $10.4^\circ$  [Fig. 4(a)]. Therefore, it is obvious that  $\text{NiCr}_2\text{O}_4$  has undergone a structural transition at 19.4 GPa. Indexing



of the high-pressure  $\text{NiCr}_2\text{O}_4$  modification led to another tetragonal structure with SG  $P4_32_12$  ( $Z = 8$ ) [Fig. 4(b)]. The  $I4_1/amd \rightarrow P4_32_12$  transition does not involve any cationic coordination increase for either  $\text{Ni}^{2+}$  or  $\text{Cr}^{3+}$  (SG  $P4_32_12$  is a subgroup of SG  $I4_1/amd$ ). Even though such phase has been observed as a low-temperature modification of  $\text{MgTi}_2\text{O}_4$ <sup>56</sup>, it is the first report of a Cr-bearing spinel adopting this particular tetragonal structure.

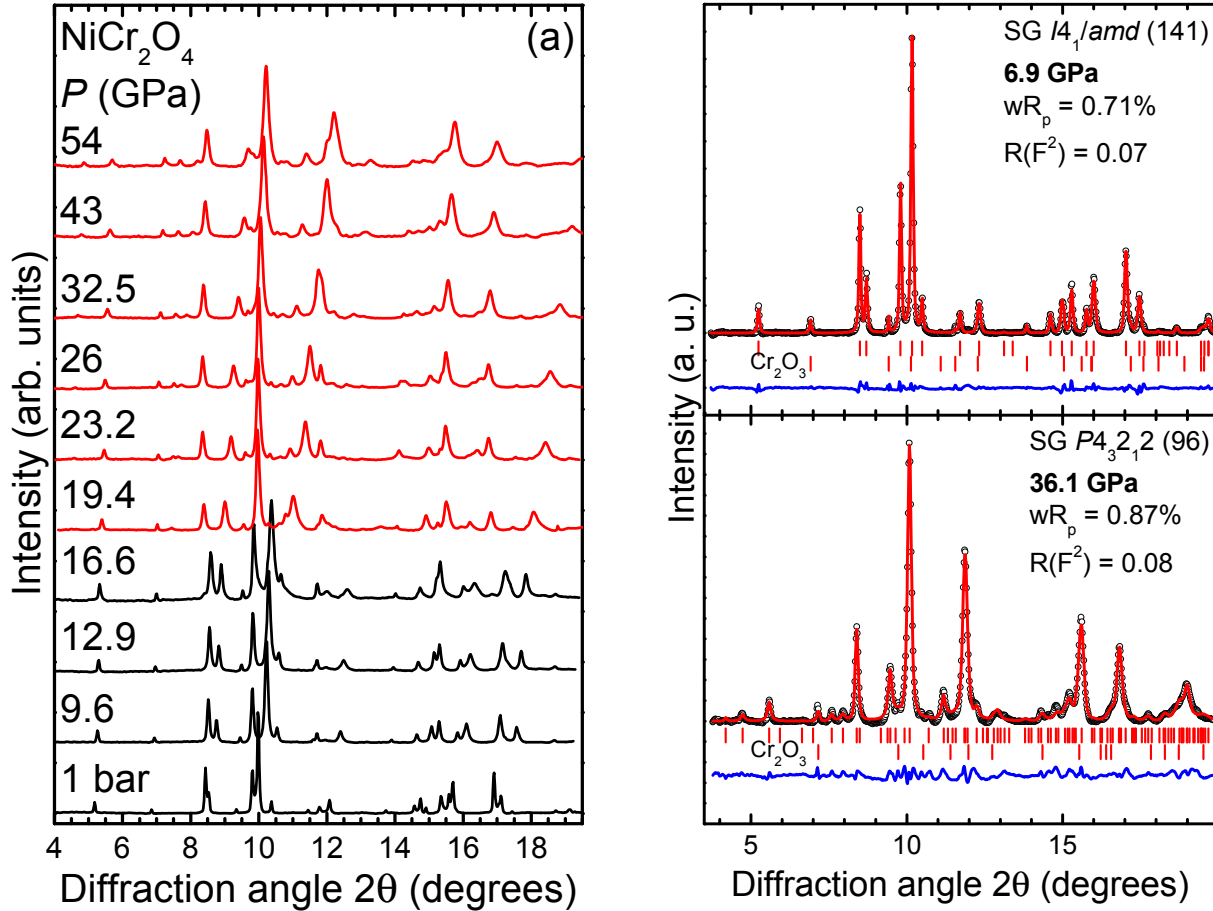


**FIG. 4.** (a) Selected XRD patterns of  $\text{NiCr}_2\text{O}_4$  at various pressures ( $T = 300$  K,  $\lambda = 0.4340$  Å). The various phases are distinguished by black ( $I4_1/amd$ ) and red ( $P4_32_12$ ) colors. (b) Examples of Rietveld refinements of  $\text{NiCr}_2\text{O}_4$  XRD patterns at 6.9 GPa (top) and at 36.1 GPa (bottom). Dots stand for the measured spectra, the red solid lines represent the best refinements, and their difference is drawn as blue lines. Vertical ticks mark the respective Bragg peak positions.

The high quality of the XRD patterns allowed for Rietveld refinements of the  $\text{NiCr}_2\text{O}_4$  diffractograms. The respective lattice parameters and atomic coordinates are provided in **Table S4** in the **Supplement**<sup>46</sup>. Here we show the tetragonal  $c/a$  axial ratio and the  $P$ - $V$  data for the two  $\text{NiCr}_2\text{O}_4$  phases (Fig. 5). As we can observe in Fig. 5(a), the tetragonal  $c/a$  axial ratio increases upon compression, indicating the enhancement of the Jahn-Teller polyhedral distortion in the

NiCr<sub>2</sub>O<sub>4</sub> *I*4<sub>1</sub>/*amd* ambient-pressure structure. We note here that the *I*4<sub>1</sub>/*amd* symmetry dictates one single Ni-O bond distance in the NiO<sub>4</sub> tetrahedra, and two Cr-O bond distances in the CrO<sub>6</sub> octahedra (two apical bonds along the long *c*-axis, and two equatorial bonds parallel to the tetragonal *ab*-plane) comprising the tetragonal spinel phase. Thus, the increase of the *c/a* ratio directly implies the elongation of the CrO<sub>6</sub> octahedra along the *c*-axis, i.e. the apical Cr-O bonds are increasing at the expense of the equatorial ones, in excellent agreement with our refined Cr-O data (Table S4 in the Supplement<sup>46</sup>). Nevertheless, the overall Jahn-Teller distortion in the starting NiCr<sub>2</sub>O<sub>4</sub> *I*4<sub>1</sub>/*amd* phase is small and is virtually eliminated upon compression, as revealed by the pressure-induced evolution of the Jahn-Teller distortion parameter  $\sigma_{JT}$ , as in the case of CuWO<sub>4</sub><sup>57,58</sup> (Fig. S3 in the Supplement<sup>46</sup>).

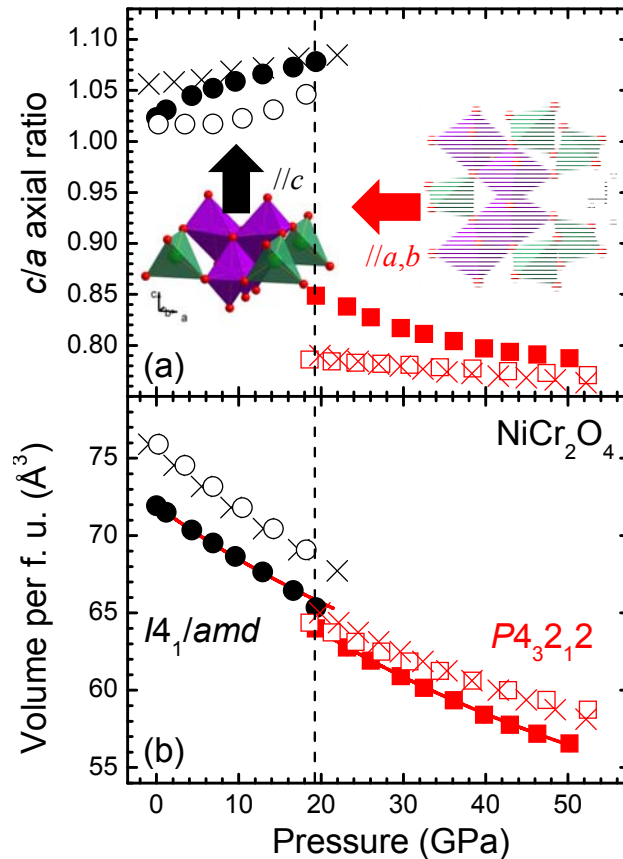


**FIG. 5.** Plot of the (a) *c/a* axial ratio and (b) volume per formula unit (f. u.) as a function of pressure for the two modifications of NiCr<sub>2</sub>O<sub>4</sub> (error bars lie within the symbols). The closed and open symbols correspond to experimental and DFT data, respectively. The vertical dashed lines depict the experimental transition pressures, and the red solid lines through the symbols indicate the fitted Birch-Murnaghan equations of state<sup>49,50</sup>. Nomenclature of the symbols is as follows: Black circles and red squares correspond to the PM *I*4<sub>1</sub>/*amd* and *P*4<sub>3</sub>2<sub>1</sub>2 phases of NiCr<sub>2</sub>O<sub>4</sub>, respectively. The black and red (X) symbols stand for the corresponding AFM *I*4<sub>1</sub>/*amd* and *P*4<sub>3</sub>2<sub>1</sub>2 phases of NiCr<sub>2</sub>O<sub>4</sub>, respectively, as obtained from DFT calculations. The obtained elastic parameters are listed in Table I. The respective lattice parameters are provided in Tables S4-S5 in the

**Supplement**<sup>46</sup>. The overall deformation of the NiCr<sub>2</sub>O<sub>4</sub> polyhedra is also drawn for clarity in panel (a).

Upon passing into the high-pressure  $P4_32_12$  phase, we can observe that the  $c/a$  ratio decreases by  $\sim 2\%$  due to the abrupt reduction of the  $c$ -axis [Fig. 5(a) and Table S4 in the Supplement<sup>46</sup>], resulting also in a  $\sim 3\%$  volume change at the  $I4_1/amd \rightarrow P4_32_12$  transition point [Fig. 5(b)], thus classifying the transition as of first-order. We can also notice that the pressure-induced  $c/a$  trend reverses in the  $P4_32_12$  phase, i.e. the equatorial Cr-O bonds expand at the expense of the apical ones. The latter observation indicates that (a) the Jahn-Teller distortion caused by the Ni<sup>2+</sup> ions persists also in the high-pressure phase, contrary to the general trend of eliminating the Jahn-Teller effect upon sufficient compression<sup>59</sup>, and (b) the overall polyhedral distortion in the high-pressure  $P4_32_12$  modification is opposite to the starting  $I4_1/amd$  one. Plotting of the Jahn-Teller distortion parameter  $\sigma_{JT}$  shows that the Jahn-Teller distortion increases one order of magnitude in the  $P4_32_12$  phase at the transition point (Fig. S3 in the Supplement<sup>46</sup>). Further compression enhances the CrO<sub>6</sub> polyhedral distortion, whereas a downturn in the pressure slope of  $\sigma_{JT}$  is detected close to 36-40 GPa. Extrapolation of the respective data indicates the complete Jahn-Teller suppression at  $\sim 120$  GPa. Given the discussion that follows below, we tend to attribute the enhancement of the Jahn-Teller distortion upon the  $I4_1/amd \rightarrow P4_32_12$  transition not as the driving force behind the observed structural change, as e.g. in the case of CuWO<sub>4</sub><sup>57,58</sup>, but rather as a *byproduct* of the magnetic changes accompanying the structural modification.

In Fig. 5(b) we plot the experimental and calculated  $P$ - $V$  data for both phases. We can immediately observe that the DFT calculated values always lie higher than their experimental counterparts, attributed to the tendency of the GGA approximation used here to overestimate the unit cell volumes and, concominantly, underestimate the bulk moduli<sup>52</sup>. Interestingly, we note that the experimental bulk modulus of the high-pressure  $P4_32_12$  phase is similar to the bulk modulus value of the starting  $I4_1/amd$  structure, implying a smaller bulk modulus for  $P4_32_12$ , i.e. the high-pressure phase of NiCr<sub>2</sub>O<sub>4</sub> appears to be *softer* than the ambient-pressure structure; this is more evident in our DFT calculations (Table I). Even though such effect is quite *unusual* in high-pressure studies, a possible cause might be underlying electronic effects due to changes in the nature of interionic bonding after the  $I4_1/amd \rightarrow P4_32_12$  transition (e.g. the Cr-O distances expand by  $\sim 6\%$ , whereas the Ni-O bond lengths shorten by  $\sim 8\%$  at the transition point), as in the case of CrN<sup>60</sup>.

Our DFT calculations in the case of NiCr<sub>2</sub>O<sub>4</sub> were performed assuming a PM and AFM  $I4_1/amd$  structures, as well as a PM and a AFM high-pressure  $P4_32_12$  phase (Table S5 in the Supplement<sup>46</sup>). Evaluation of the respective enthalpies indicates that the AFM  $I4_1/amd$  structure adopts the PM  $P4_32_12$  phase close to 25 GPa (Fig. 6), in good agreement with the experimental value, whereas the PM  $I4_1/amd$  phase transforms into the PM  $P4_32_12$  phase close to 35 GPa (the AFM  $P4_32_12$  phase is adopted in both cases 5 GPa higher than the PM one, Fig. 6 and Fig. S3 in the Supplement<sup>46</sup>). Except from the reasons reported earlier regarding the temperature effect, as

well as the overestimation of the volume within the GGA approximation, it appears also that the calculated transition pressure depends also on the choice of the exact magnetic configuration. The latter enlightens the inconsistencies in the experimental and calculated transition pressures in the case of  $\text{MnCr}_2\text{O}_4$ , as we discuss in more detail in the next *Section*.

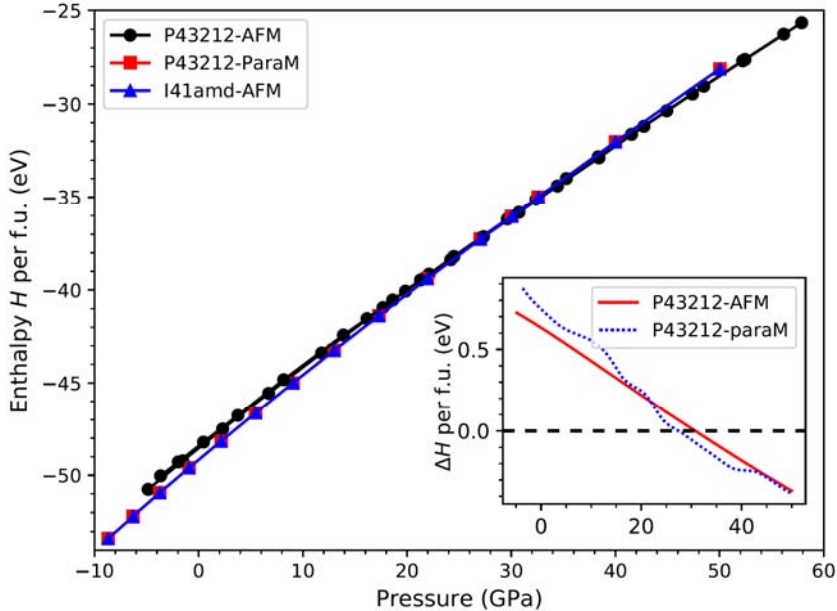


**FIG. 6:** The calculated enthalpies of the  $I4_1/amd$  (AFM, blue), the  $P4_32_12$ -AFM (black), and the  $P4_32_12$ -ParaM (red)  $\text{NiCr}_2\text{O}_4$  phases as a function of pressure. Inset: the enthalpy difference between the  $P4_32_12$  (AFM and paraM) and  $I4_1/amd$  (AFM) phases with respect to pressure. Enthalpy  $H$  is defined as  $H(P) = E + PV$ , and a phase is stable if it has a lower value of  $H$ . The  $I4_1/amd$ -AFM  $\rightarrow$   $P4_32_12$ -ParaM transition takes place at 25 GPa, whereas the  $I4_1/amd$ -AFM  $\rightarrow$   $P4_32_12$ -AFM transition is estimated at 30 GPa.

### C. Pressure-induced structural transition and magnetic exchange in Cr-spinels

Having established the transition pressures ( $P_{\text{Tr}}$ ) for both  $\text{MnCr}_2\text{O}_4$  and  $\text{NiCr}_2\text{O}_4$  spinels, we turn now to some common aspects of the (first) pressure-induced structural transition in the Cr-spinel series. Comparison of the available literature reveals that for sulfide and selenide Cr-spinels, the cubic  $\rightarrow$  tetragonal transition is always accompanied by a volume decrease of 4-5% at the transition point<sup>19-23,61</sup>. In addition, DFT calculations have identified concomitant magnetic changes accompanying these structural transitions, i.e. from the starting FM states towards AFM ones<sup>20-22</sup>. Taken together, we were able to identify a linear relationship between the  $P_{\text{Tr}}$  of Cr-bearing spinel sulfides and selenides and the  $K_{\text{nnn}}/J_{\text{nn}}$  ratio of next-nearest neighbor  $K_{\text{nnn}}$  to nearest neighbor  $J_{\text{nn}}$   $\text{Cr}^{3+}$  magnetic exchange interactions<sup>19,20</sup>.

Given, however, that the  $K_{\text{nm}}$  interactions are not relevant for Cr-oxide spinels bearing magnetic  $A^{2+}$  cations<sup>2,4,18</sup>, does a similar relation between  $P_{\text{Tr}}$  and magnetic exchange interactions **hold for** these materials? For this purpose, we have calculated the relevant magnetic exchange parameters  $J_{\text{AA}}$ ,  $J_{\text{BB}}$ , and  $J_{\text{AB}}$  for the whole spinel series with magnetic  $A^{2+}$  cations ( $A^{2+} = \text{Mn-Cu}$ ) at ambient pressure, the most important magnetic parameters in these compounds<sup>4,18</sup>. All of these data, alongside relevant literature values<sup>4,18,62,63</sup>, are listed in **Table S8** in the **Supplement**<sup>46</sup>. We note that  $J_{\text{AA}}$  represents the interactions between  $A^{2+}$  cations,  $J_{\text{AB}}$  denotes the magnetic exchange between  $A^{2+}$  and  $\text{Cr}^{3+}$ , and  $J_{\text{BB}}$  stands for  $\text{Cr}^{3+}$ - $\text{Cr}^{3+}$  interactions.

In **Fig. 7** we plot the calculated  $J_{\text{BB}}$  exchange parameter as a function of  $P_{\text{Tr}}$  for all the relevant spinels. We can immediately observe a linear dependence of the two parameters, with the exception of  $\text{CuCr}_2\text{O}_4$  which does not show any transition up to 50 GPa, whereas the  $P_{\text{Tr}} = 25$  GPa in this case indicates an isostructural transition, most likely resulting from a pressure-induced orbital reorientation<sup>24</sup>. We note also that the calculated magnetic exchange interactions of  $\text{CuCr}_2\text{O}_4$  are much larger compared to the rest of the spinels (**Table S8** in the **Supplement**<sup>46</sup>), possibly accounting for the absence of any structural transition up to 50 GPa<sup>24</sup>. On the other hand,  $\text{CoCr}_2\text{O}_4$  undergoes a structural distortion at about 16 GPa, attributed to magnetic frustration<sup>45</sup>. Moreover,  $\text{FeCr}_2\text{O}_4$  has been studied up to 93 GPa<sup>64,65</sup>. These studies established a  $Fd\bar{3}m \rightarrow I4_1/amd$  structural transition close to 12 GPa in  $\text{FeCr}_2\text{O}_4$  due to Jahn-Teller effects. Further compression leads to  $\text{Fe} \leftrightarrow \text{Cr}$  intercationic site exchange and a high-spin to low-spin state transition of divalent  $\text{Fe}^{64}$ . We should also note here that the  $P_{\text{Tr}}$  of several ternary  $\text{AB}_2\text{X}_4$  compounds was shown to depend on the cationic radii ratio of the respective constituent ions<sup>66,67</sup>; such relationship, however, does not seem to hold for Cr-bearing spinels [see **Fig. 10** in Ref.<sup>20</sup>].

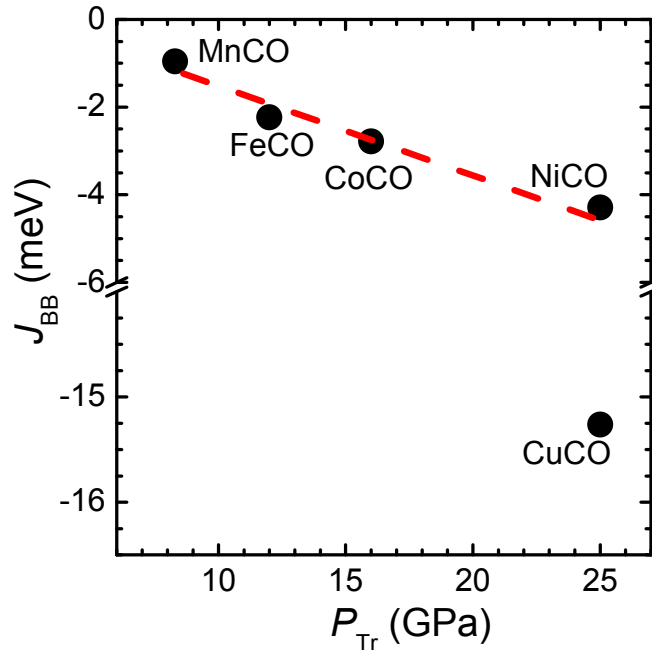


**FIG. 7.** Plot of the  $J_{BB}$  magnetic exchange interaction against the transition pressure  $P_{Tr}$  for the Cr-spinels with magnetic  $A^{2+}$  cations. The compound abbreviations are as follows:  $MnCr_2O_4 \rightarrow MnCO$ ,  $FeCr_2O_4 \rightarrow FeCO$ ,  $CoCr_2O_4 \rightarrow CoCO$ ,  $NiCr_2O_4 \rightarrow NiCO$ , and  $CuCr_2O_4 \rightarrow CuCO$  (**Table S8** in the **Supplement**<sup>46</sup>).

From our plot (**Fig. 7**) it becomes immediately evident that the structural distortions/transitions observed in the Cr-spinel series are closely interrelated to magnetic rather than steric or Jahn-Teller effects. Considering our aforementioned results on spinel sulfides and selenides with non-magnetic  $A^{2+}$  cations, we can generally state at this point that *the structural transitions in Cr-based spinels are intimately connected with the Cr-Cr magnetic exchange interactions*.

In order to link our suggestion with the theory developed by Lyons, Kaplan, Dwight, and Menyuk (LKDM) for these systems<sup>2</sup>, the magnetic ground state and/or the magnetic frustration of a cubic spinel compound can be described by the parameter  $u$ :

$$u = \frac{4J_{BB}S_B}{3J_{AB}S_A} \quad (1)$$

where  $S_A$  and  $S_B$  denote the spin magnitude of the A and B cations in the  $AB_2X_4$  spinel phase<sup>68</sup>. It is clear that the parameter  $u$  represents the relative strength between the two different nearest neighbor interactions  $J_{BB}$  and  $J_{AB}$ . According to LKDM, the numerical value of  $u$  describes the magnetic ground state of the spinel, with  $u \leq 8/9$  denoting a collinear AFM Néel state (e.g. all A-site spins parallel to each other and antiparallel to the B-site spins),  $8/9 < u < 1.298$  a ferrimagnetic spiral configuration, whereas for  $u > 1.298$  the latter ferrimagnetic configuration becomes unstable resulting in an unstable spiral state. Therefore, it becomes clear that the larger the magnitude of  $u$ , the more magnetically unstable the respective spinel becomes. Given that the  $J_{BB}$  coupling constant displays a larger enhancement under pressure compared to  $J_{AB}$  (**Fig. 8**, see also **Table I** in Ref. <sup>45</sup>], we can reasonably anticipate the enhancement of the magnetic instability in these systems under compression. Consequently, it appears that this built-up pressure-induced magnetic instability is partially relieved by structural transitions in these materials, leading possibly also to the realization of new magnetic ground states<sup>20,45,64</sup>.

Indeed, our DFT calculations have revealed that the structural transitions may be accompanied by magnetic ones in both  $MnCr_2O_4$  and  $NiCr_2O_4$  spinels. Regarding the former, we mentioned earlier the discrepancies between the experimental and calculated  $P_{Tr}$  for the observed structural transitions. Considering the sensitivity of the calculated enthalpy on the choice of the exact magnetic configuration (see the  $NiCr_2O_4$  discussion earlier), one possible explanation behind the  $P_{Tr}$  discrepancies might be that the selected tetragonal AFM-MnCr and AFM-Cr states might not be the most suitable candidates for describing the  $MnCr_2O_4$  magnetic configurations under pressure. More complex magnetic ground states with tetragonal symmetries might be needed for this purpose, a task which lies beyond the scope of the present manuscript.

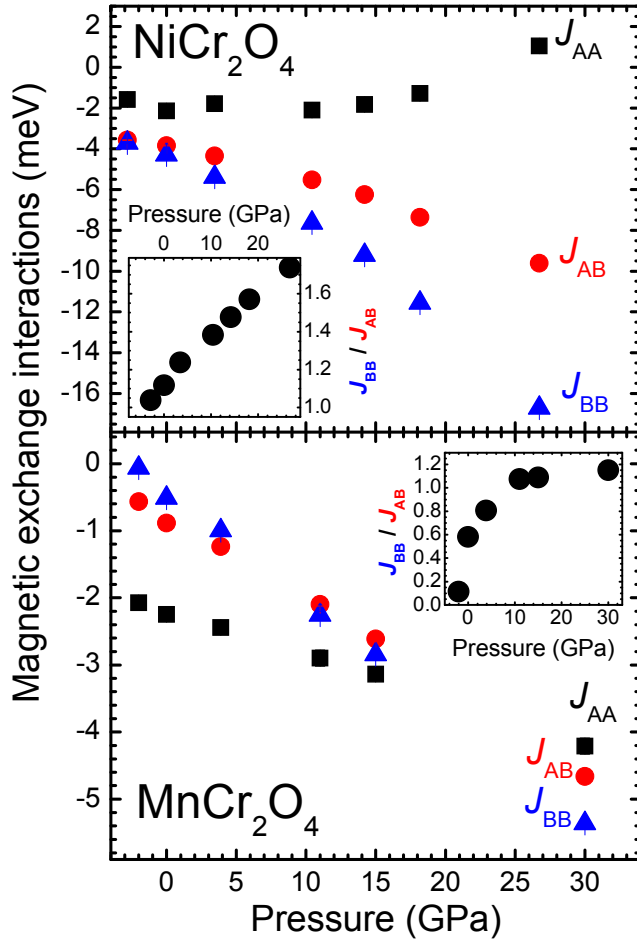


**FIG. 8:** Plot of the various magnetic exchange interactions for the ambient-pressure cubic and tetragonal  $\text{MnCr}_2\text{O}_4$  (bottom) and  $\text{NiCr}_2\text{O}_4$  (top) as a function of pressure. Even though the respective pressure stability fields of the original phases is up to  $\sim 8$  GPa and  $\sim 20$  GPa, respectively, we have expanded the calculations to higher pressures for clarity. The insets depict the respective  $J_{\text{BB}}/J_{\text{AB}}$  ratios.

Finally, we consider it interesting to compare the present results on Cr-spinels with the recent high-pressure studies conducted on the  $\text{A}^{2+}\text{V}_2\text{O}_4$  spinels ( $\text{A}^{2+} = \text{Mg, Mn, Fe, Co, Zn, Cd}$ )<sup>11,53</sup>. Compared to the  $\text{Cr}^{3+}$ -bearing oxospinel with localized  $3d_{t_2g}$  electrons ( $\text{Cr}^{3+} 3d^3$ ;  $S = 3/2$ ) and large electronic band gaps, the  $\text{V}^{3+}$ -bearing spinels ( $\text{V}^{3+} 3d^2$ ;  $S = 1$ ) are closer to a localized-itinerant transition under compression<sup>11,69</sup>. Interestingly, such an electronic transition was speculated to take place at a critical intermetallic separation distance  $R_c$  between the  $\text{Cr}^{3+}$ - $\text{Cr}^{3+}$  ( $R_c = 2.84$  Å) and the  $\text{V}^{3+}$ - $\text{V}^{3+}$  ( $R_c = 2.97$  Å) cations<sup>5,70</sup>. For the  $\text{V}^{3+}$ -spinels, however, the proposed  $R_c$  appears to be overestimated<sup>53</sup>. This appears to be the case also for the Cr-bearing oxospinel, as e.g. the intermetallic  $\text{Cr}^{3+}$ - $\text{Cr}^{3+}$  distance in  $\text{CoCr}_2\text{O}_4$  reaches  $R_c = 2.84$  Å close to 30 GPa, but without any indication of a metallic transition<sup>45</sup>. Moreover, the high-pressure  $P4_32_12$  modification of  $\text{NiCr}_2\text{O}_4$  exhibits an intermetallic  $\text{Cr}^{3+}$ - $\text{Cr}^{3+}$  distance of 2.6 Å close to 50 GPa,

again with no indication of metallization (at least visually). Hence, the concept of a critical intermetallic separation distance leading to localized-to-itinerant transitions in transition metal compounds should be revisited.

#### IV. CONCLUSIONS

In summary, we have investigated the high-pressure structural behavior of the  $\text{MnCr}_2\text{O}_4$  and  $\text{NiCr}_2\text{O}_4$  spinels at room temperature. In both cases, we have unraveled pressure-induced structural transitions into tetragonal modifications. In the case of  $\text{MnCr}_2\text{O}_4$ , the structural transitions did not result in sizeable volume changes at the respective transition points. On the other hand,  $\text{NiCr}_2\text{O}_4$  undergoes a first-order  $I4_1/amd \rightarrow P4_32_12$  transition with a reversal of the  $c/a$  axial ratio slope, indicating opposite Jahn-Teller effects in the two structures.

Considering the present results, we all as the available literature, we have shown that the Cr-oxide spinels with magnetic  $A^{2+}$  cations ( $A^{2+} = \text{Mn, Fe, Co, Ni, Cu}$ ) follow a similar trend as their chalcogenide counterparts with non-magnetic  $A^{2+}$  ions, i.e. the transition pressure is proportional to the magnitude of the Cr-Cr magnetic exchange interactions active in these compounds. Therefore, we have reached the conclusion that *knowing the Cr-Cr magnetic exchange interactions alone suffices to account for the high-pressure behavior of these systems*. It would be interesting to search for analogous interrelations of magnetic and structural properties in relevant material families.

#### ACKNOWLEDGMENTS

We would like to thank Dr. D. Popov for his assistance with the XRD measurements, and Dr. S. Tkachev at GeoSoilEnviroCARS (Sector 13), APS-ANL for his assistance with the DAC gas loading. Portions of this work were performed at HPCAT (Sector 16), Advanced Photon Source (APS), Argonne National Laboratory. HPCAT operations are supported by DOE-NNSA under Award No. DE-NA0001974 and DOE-BES under Award No. DE-FG02-99ER45775, with partial instrumentation funding by NSF. The Advanced Photon Source is a U.S. Department of Energy (DOE) Office of Science User Facility operated for the DOE Office of Science by Argonne National Laboratory under Contract No. DE-AC02-06CH11357. Portions of this work were performed at GeoSoilEnviroCARS (The University of Chicago, Sector 13), Advanced Photon Source (APS), Argonne National Laboratory. GeoSoilEnviroCARS is supported by the National Science Foundation - Earth Sciences (EAR-1128799) and Department of Energy-GeoSciences (DE-FG02-94ER14466). This research used resources of the Advanced Photon Source, a U.S. Department of Energy (DOE) Office of Science User Facility operated for the DOE Office of Science by Argonne National Laboratory under Contract No. DE-AC02-



06CH11357. Use of the COMPRES-GSECARS gas loading system was supported by COMPRES under NSF Cooperative Agreement EAR 11-57758 and by GSECARS through NSF grant EAR-1128799 and DOE grant DE-FG02-94ER14466. This research used resources of the Advanced Photon Source, a U.S. Department of Energy (DOE) Office of Science User Facility operated for the DOE Office of Science by Argonne National Laboratory under Contract No. DE-AC02-06CH11357. We are grateful to the Michigan Space Grant Consortium for supporting this research. We acknowledge use of computational resources from the Tandy Supercomputing Center and the Ohio Supercomputing Center<sup>71</sup>. We acknowledge support from the NSF CMMI 1629239 grants. This research has been partially supported by the Deutsche Forschungsgemeinschaft (DFG) via the Transregional Collaborative Research Center TRR 80 (Augsburg-Munich).

<sup>1</sup> P.K. Baltzer, P.J. Wojtowicz, M. Robbins, and E. Lopatin, *Phys. Rev.* **151**, 367 (1966).

<sup>2</sup> D.H. Lyons, T.A. Kaplan, K. Dwight, and N. Menyuk, *Phys. Rev.* **126**, 540 (1962).

<sup>3</sup> T. Rudolf, C. Kant, F. Mayr, J. Hemberger, V. Tsurkan, and A. Loidl, *New J. Phys.* **9**, 76 (2007).

<sup>4</sup> D. Das and S. Ghosh, *J. Phys. D Appl. Phys.* **48**, 425001 (2015).

<sup>5</sup> J.B. Goodenough, *Magnetism and the Chemical Bond* (John Wiley and sons, 1963).

<sup>6</sup> J.B. Goodenough, *Phys. Rev.* **117**, 1442 (1960).

<sup>7</sup> J.B. Goodenough, *J. Phys. Chem. Sol.* **6**, 287 (1958).

<sup>8</sup> D.G. Wickham and J.B. Goodenough, *Phys. Rev.* **115**, 1156 (1959).

<sup>9</sup> J.D. Dunitz and L.E. Orgel, *J. Phys. Chem. Sol.* **3**, 20 (1957).

<sup>10</sup> J.B. Goodenough and A.L. Loeb, *Phys. Rev.* **98**, 391 (1955).

<sup>11</sup> S. Blanco-Canosa, F. Rivadulla, V. Pardo, D. Baldomir, J.-S. Zhou, M. Garcia-Hernandez, M.A. Lopez-Quintela, J. Rivas, and J.B. Goodenough, *Phys. Rev. Lett.* **99**, 187201 (2007).

<sup>12</sup> H. Ueda and Y. Ueda, *Phys. Rev. B* **77**, 224411 (2008).

<sup>13</sup> S. Rahman, S. Samanta, D. Errandonea, S. Yan, K. Yang, J. Lu, and L. Wang, *Phys. Rev. B* **95**, 024107 (2017).

- <sup>14</sup> P. Kistaiah, K.S. Murthy, and K.V.K. Rao, *J. Less-Com. Met.* **98**, L13 (1984).
- <sup>15</sup> S.-D. Guo and B.-G. Liu, *J. Phys. Cond. Matt.* **24**, 45502 (2012).
- <sup>16</sup> Y. Amiel, G.K. Rozenberg, N. Nissim, A. Milner, M.P. Pasternak, M. Hanfland, and R.D. Taylor, *Phys. Rev. B* **84**, 224114 (2011).
- <sup>17</sup> S. Rahman, H. Saqib, J. Zhang, D. Errandonea, C. Menendez, C. Cazorla, S. Samanta, X. Li, J. Lu, and L. Wang, *Phys. Rev. B* **97**, 174102 (2018).
- <sup>18</sup> C. Ederer and M. Komelj, *Phys. Rev. B* **76**, 064409 (2007).
- <sup>19</sup> I. Efthimiopoulos, T. Lochbiler, V. Tsurkan, A. Loidl, V. Felea, and Y. Wang, *J. Phys. Chem. C* **121**, 769-777 (2017).
- <sup>20</sup> I. Efthimiopoulos, Z.T.Y. Liu, M. Kucway, S. V Khare, P. Sarin, V. Tsurkan, A. Loidl, and Y. Wang, *Phys. Rev. B* **94**, 174106 (2016).
- <sup>21</sup> I. Efthimiopoulos, A. Yaresko, V. Tsurkan, J. Deisenhofer, A. Loidl, C. Park, and Y. Wang, *Appl. Phys. Lett.* **103**, 201908 (2013).
- <sup>22</sup> I. Efthimiopoulos, A. Yaresko, V. Tsurkan, J. Deisenhofer, A. Loidl, C. Park, and Y. Wang, *Appl. Phys. Lett.* **104**, 11911 (2014).
- <sup>23</sup> I. Efthimiopoulos, Z.T.Y. Liu, S. V Khare, P. Sarin, V. Tsurkan, A. Loidl, D. Popov, and Y. Wang, *Phys. Rev. B* **93**, 174103 (2016).
- <sup>24</sup> I. Efthimiopoulos, V. Tsurkan, A. Loidl, D. Zhang, and Y. Wang, *J. Phys. Chem. C* **121**, 16513 (2017).
- <sup>25</sup> K. Dey, S. Majumdar, and S. Giri, *Phys. Rev. B* **90**, 184424 (2014).
- <sup>26</sup> J. Barman, T. Bora, and S. Ravi, *J. Magn. Magn. Mater.* **385**, 93 (2015).
- <sup>27</sup> K. Syassen, *High Press. Res.* **28**, 75 (2008).
- <sup>28</sup> D. Zhang, P.K. Dera, P.J. Eng, J.E. Stubbs, J.S. Zhang, V.B. Prakapenka, and M.L. Rivers, *J. Vis. Exp.* **119**, e54660 (2017).
- <sup>29</sup> P.W. Stephens, *J. Appl. Cryst.* **32**, 281 (1999).

- <sup>30</sup> R.B. von Dreele, *J. Appl. Cryst.* **30**, 517 (1997).
- <sup>31</sup> G. Kresse and J. Furthmüller, *Comput. Mater. Sci.* **6**, 15 (1996).
- <sup>32</sup> G. Kresse and J. Furthmüller, *Phys. Rev. B* **54**, 11169 (1996).
- <sup>33</sup> G. Kresse and J. Hafner, *Phys. Rev. B* **49**, 14251 (1994).
- <sup>34</sup> G. Kresse and J. Hafner, *Phys. Rev. B* **47**, 558 (1993).
- <sup>35</sup> G. Kresse and D. Joubert, *Phys. Rev. B* **59**, 1758 (1999).
- <sup>36</sup> P.E. Blöchl, *Phys. Rev. B* **50**, 17953 (1994).
- <sup>37</sup> J.P. Perdew, J.A. Chevary, S.H. Vosko, K.A. Jackson, M.R. Pederson, D.J. Singh, and C. Fiolhais, *Phys. Rev. B* **46**, 6671 (1992).
- <sup>38</sup> L. Wang, T. Maxisch, and G. Ceder, *Phys. Rev. B* **73**, 195107 (2006).
- <sup>39</sup> A. Jain, G. Hautier, S.P. Ong, C.J. Moore, C.C. Fischer, K.A. Persson, and G. Ceder, *Phys. Rev. B* **84**, 045115 (2011).
- <sup>40</sup> A. van de Walle, P. Tiwary, M. de Jong, D.L. Olmsted, M. Asta, A. Dick, D. Shin, Y. Wang, L.-Q. Chen, and Z.-K. Liu, *Calphad-Computer Coupling Phase Diagrams Thermochem.* **42**, 13 (2013).
- <sup>41</sup> A. Zunger, S.H. Wei, L.G. Ferreira, and J.E. Bernard, *Phys. Rev. Lett.* **65**, 353 (1990).
- <sup>42</sup> A. van de Walle, M. Asta, and G. Ceder, *Calphad-Computer Coupling Phase Diagrams Thermochem.* **26**, 539 (2002).
- <sup>43</sup> A. van de Walle, *Calphad-Computer Coupling Phase Diagrams Thermochem.* **33**, 266 (2009).
- <sup>44</sup> I. Efthimiopoulos, J. Kemichick, X. Zhou, S. V Khare, D. Ikuta, and Y. Wang, *J. Phys. Chem. A* **118**, 1713 (2014).
- <sup>45</sup> I. Efthimiopoulos, Z.T.Y. Liu, S. V Khare, P. Sarin, T. Lochbiler, V. Tsurkan, A. Loidl, D. Popov, and Y. Wang, *Phys. Rev. B* **92**, 064108 (2015).
- <sup>46</sup> See Supplemental Material at [for the complete set of experimental and calculated structural parameters, as well as the list of magnetic data used for our DFT calculations. An overview Table for all relevant spinels are supplied also for convenience.](#)

- <sup>47</sup> S. Klotz, J.-C. Chervin, P. Munsch, and G. Le Marchand, *J. Phys. D Appl. Phys.* **42**, 75413 (2009).
- <sup>48</sup> W. Yong, S. Botis, S.R. Shieh, W. Shi, and A.C. Withers, *Phys. Earth Planet. Inter.* **196–197**, 75 (2012).
- <sup>49</sup> F. Birch, *Phys. Rev.* **71**, 809 (1947).
- <sup>50</sup> F. Birch, *J. Geophys. Res.* **83**, 1257 (1978).
- <sup>51</sup> K. Tomiyasu, J. Fukunaga, and H. Suzuki, *Phys. Rev. B* **70**, 214434 (2004).
- <sup>52</sup> S. Baroni, S. de Gironcoli, A.D. Corso, and P. Giannozzi, *Rev. Mod. Phys.* **73**, 515 (2001).
- <sup>53</sup> Z.-Y. Li, X. Li, J.-G. Cheng, L.G. Marshall, X.-Y. Li, A.M. dos Santos, W.-G. Yang, J.J. Wu, J.-F. Lin, G. Henkelman, T. Okada, Y. Uwatoko, H.B. Cao, H.D. Zhou, J.B. Goodenough, and J.-S. Zhou, *Phys. Rev. B* **94**, 165159 (2016).
- <sup>54</sup> P.G. Radaelli, *New J. Phys.* **7**, 53 (2005).
- <sup>55</sup> M.R. Suchomel, D.P. Shoemaker, L. Ribaud, M.C. Kemei, and R. Seshadri, *Phys. Rev. B* **86**, 054406 (2012).
- <sup>56</sup> M. Schmidt, W. Ratcliff III, P.G. Radaelli, K. Refson, N.M. Harrison, and S.W. Cheong, *Phys. Rev. Lett.* **92**, 056402 (2004).
- <sup>57</sup> J. Ruiz-Fuertes, A. Friedrich, J. Pellicer-Porres, D. Errandonea, A. Segura, W. Morgenroth, E. Haussuhl, C.-Y. Tu, and A. Polian, *Chem. Mater.* **23**, 4220 (2011).
- <sup>58</sup> J. Ruiz-Fuertes, A. Segura, F. Rodriguez, D. Errandonea, and M.N. Sanz-Ortiz, *Phys. Rev. Lett.* **108**, 166402 (2012).
- <sup>59</sup> I. Loa, P. Adler, A. Grzechnik, K. Syassen, U. Schwarz, M. Hanfland, G.K. Rozenberg, P. Gorodetsky, and M.P. Pasternak, *Phys. Rev. Lett.* **87**, 125501 (2001).
- <sup>60</sup> F. Rivadulla, M. Banobre-Lopez, C.X. Quintela, A. Pineiro, V. Pardo, D. Baldomir, M.A. Lopez-Quintela, J. Rivas, C.A. Ramos, H. Salva, J.-S. Zhou, and J.B. Goodenough, *Nat. Mater.* **8**, 947 (2009).
- <sup>61</sup> I. Efthimiopoulos, *High-Pressure Structural and Spectroscopic Studies on Transition Metal Compounds*, Ph.D. thesis, Aristotle University of Thessaloniki (2010).

- <sup>62</sup> B.C. Melot, J.E. Drewes, R. Seshadri, E.M. Stoudenmire, and A.P. Ramirez, *J. Phys. Cond. Matt.* **21**, 216007 (2009).
- <sup>63</sup> E. Winkler, S. Blanco-Canosa, F. Rivadulla, M.A. Lopez-Quintela, J. Rivas, A. Caneiro, M. T. Causa, and M. Tovar, *Phys. Rev. B* **80**, 104418 (2009).
- <sup>64</sup> W.M. Xu, G.R. Hearne, S. Layek, D. Levy, J.-P. Itie, M.P. Pasternak, G.K. Rozenberg, and E. Greenberg, *Phys. Rev. B* **95**, 045110 (2017).
- <sup>65</sup> A. Kyono, S.A. Gramsch, T. Yamanaka, D. Ikuta, M. Ahart, B.O. Mysen, H.K. Mao, and R.J. Hemley, *Phys. Chem. Miner.* **39**, 131 (2012).
- <sup>66</sup> F.J. Manjon and R.I. Vilaplana, *Pressure-Induced Phase Transitions in AB<sub>2</sub>X<sub>4</sub> Chalcogenide Compounds* (Springer-Verlag Berlin Heidelberg, 2014).
- <sup>67</sup> D. Errandonea, R.S. Kumar, F.J. Manjon, V. V Ursaki, and I.M. Tiginyanu, *J. Appl. Phys.* **104**, 63524 (2008).
- <sup>68</sup> D. Louer and R. Vargas, *J. Appl. Crystallogr.* **15**, 542 (1982).
- <sup>69</sup> A. Kismarahardja, J.S. Brooks, A. Kiswandhi, K. Matsubayashi, R. Yamanaka, Y. Uwatoko, J. Whalen, T. Siegrist, and H.D. Zhou, *Phys. Rev. Lett.* **106**, 056602 (2011).
- <sup>70</sup> D.B. Rogers, R.J. Arnott, A. Wold, and J.B. Goodenough, *J. Phys. Chem. Sol.* **24**, 347 (1963).
- <sup>71</sup> Ohio Supercomputer Center, <http://osc.edu/ark:/19495/f5s1ph73>